anatomical/topographic classification in 1002 consecutive patients. *Ann Surg.* 2000;232:353–61.
6. Fang WL, Wu CW, Chen JH, et al. Esophagogastric junction adenocarcinoma according to Siewert classification in Taiwan. *Ann Surg Oncol.* 2009;16:3237–44.
7. Hasegawa S, Yoshikawa T, Cho H, Tsuburaya A, Kobayashi O. Is adenocarcinoma of the esophagogastric junction difference between Japan and Western countries? The incidence and clinicopathological features at a Japanese high-volume cancer center. *World J Surg.* 2009;33:95–103.
8. Kodera Y, Yamamura Y, Shimizu Y, et al. Adenocarcinoma of the gastroesophageal junction in Japan: relevance of Siewert's classification applied to 177 cases resected at a single institution. *J Am Coll Surg.* 1999;189:594–601.
9. Yuasa N, Miyake H, Yamada T, Ebata T, Nimura Y, Hattori T. Clinicopathologic comparison of Siewert type II and III adenocarcinoma of the gastroesophageal junction. *World J Surg.* 2006;30:364–71.
10. American Joint Committee on Cancer. AJCC cancer staging manual. 7th ed. New York: Springer-Verlag; 2009.
11. Borrmann R. Geshwulste des Magens und Duodenums. In: Henke F, Lubarsh O, editors. Handbuch der Spezieller Pathologischen Anatomie und Histologie. vol. 4, pt 1. Berlin: Springer; 1926. p. 865.
12. Japanese Gastric Cancer Association. Japanese classification of gastric carcinoma. *Gastric Cancer.* 1998;1:10–24.
13. Sasako M, McCulloch P, Kinoshita T, Maruyama K. New method to evaluate the therapeutic value of lymph-node dissection for gastric cancer. *Br J Surg.* 1995;82:346–51.
14. Bai JG, Lv Y, Dang CX. Adenocarcinoma of the esophagogastric junction in China according to Siewert's classification. *Jpn J Clin Oncol.* 2006;36:364–7.
15. American Joint Committee on Cancer. AJCC cancer staging manual. 6th ed. New York: Springer-Verlag; 2002.
16. Sasako M, Sano T, Yamamoto S, et al. Left thoracoabdominal approach versus abdominal-transhiatal approach for gastric cancer of the cardia or subcardia: a randomized controlled trial. *Lancet Oncol.* 2006;7:644–51.
17. Sakuramoto S, Sasako M, Yamaguchi T, et al. Adjuvant chemotherapy for gastric cancer with S-1, an oral fluoropyrimidine. *N Engl J Med.* 2007;57:1810–20.
18. Cunningham D, Allum WH, Stenning SP, et al. Perioperative chemotherapy versus surgery alone for resectable gastroesophageal cancer. *N Engl J Med.* 2006;355:11–20.

World J Surg (2011) 35:2717–2722
DOI 10.1007/s00268-011-1269-2

Predictive Value of Baseline Neutrophil/Lymphocyte Ratio for T4 Disease in Wall-Penetrating Gastric Cancer

Masaki Aizawa · Naoto Gotohda · Shinichiro Takahashi · Masaru Konishi · Taira Kinoshita

Published online: 13 September 2011
© Société Internationale de Chirurgie 2011

Abstract
Background Multimodality therapy has been used in the management of gastric cancer associated with locoregional spread. However, the accurate clinical staging still remains to be established. The neutrophil/lymphocyte ratio (NLR) in the peripheral blood is reported to be an easily assessable prognostic factor in cancer patients. We evaluated the predictive significance of the NLR and other serological parameters in patients with wall-penetrating gastric cancer.
Methods Two hundred sixty-two patients who underwent gastric cancer surgery between 2002 and 2005 were identified retrospectively. Wall penetration was defined as wall invasion deeper than the muscularis propria (≥T2). Blood data were collected from routinely performed blood examinations before treatment and were analyzed with respect to T stage, nodal status, and histological features. A high NLR was defined as less than 3.2 based on ROC curve analysis, and the predictive value of a high NLR for T4 cancer was evaluated.
Results Elevated levels of NLR ($P = 0.004$) and C-reactive protein (CRP) ($P = 0.017$) and the decrease in lymphocyte count (Lym, $P = 0.032$) and serum hemoglobin (Hb, $P < 0.001$) were correlated with the T stage, but there was no meaningful correlation with either positive nodal status or histological differentiation. With respect to the predictive value for stage T4, an elevated NLR (OR = 2.206, 95% CI = 1.187–4.100; $P = 0.012$), decrease of Hb (OR = 1.875, 95% CI = 1.005–3.500; $P = 0.048$), and poorly differentiated histology (OR = 3.134, 95% CI = 1.593–6.167; $P = 0.001$) were identified as independent predictive factors.
Conclusion Our findings suggest that the preoperative values of the NLR may be reliable for predicting T4 disease.

M. Aizawa (✉) · N. Gotohda · S. Takahashi · M. Konishi · T. Kinoshita
Department of Surgery, National Cancer Center Hospital East, 6-5-1 Kashiwanoha, Kashiwa, Japan
e-mail: maizawa@niigata-cc.jp

Introduction

Gastric cancer is the second leading cause of cancer-related death worldwide. Annually, around 930,000 cases are diagnosed and approximately 700,000 deaths occur [1]. In Japan, the 5-year survival rate of gastric cancer patients has reached nearly 60%, attributable in part to early detection via screening [2, 3]. Though the treatment for patients with locoregional spread is still a challenge, the outcomes have lately improved with the introduction of multimodality therapies [4–6]. In particular, neoadjuvant therapies are in the limelight, with verification of their efficacy and safety under way. Therefore, precise clinical staging is considered crucial for appropriate treatment. At present, the outcome prediction is based predominantly on the TNM classification of the cancer [7]. Novel developments in imaging modalities have improved the diagnostic accuracy of the clinical stage. With respect to T staging, multidetector-row computed tomography (MDCT) with accuracy rates of 76–93% has been demonstrated to be a superior tool to endoscopic ultrasound (EUS) [8–11]. However, treatment plans occasionally need to be altered at laparotomy, indicating the superior effectiveness of staging laparoscopy [12].

Recently, the contribution of host inflammatory reactions to cancer development has been reported [13]. In particular, tumor growth-promoting infiltration by inflammatory cells and adjacent tissue remodeling are influenced

by paracrine and autocrine loops of chemokine and cytokines [14]. Though the detailed mechanism still remains unclear, the addition of inflammatory-based optional factors to the TNM classification would be expected to help in the management. Indeed, several studies have investigated the role of the immune system in the growth progression or cessation of gastric cancers, and hematological and biochemical parameters have been suggested as simply assessable indices of the systemic pathophysiologic status [15–22]. In this study we evaluated whether preoperative peripheral blood parameters are useful in predicting locoregional extension in gastric cancer patients.

Patients and methods

Patients

The cases of 872 patients with gastric cancer who had undergone surgery at the National Cancer Center Hospital East between January 2002 and December 2005 were retrospectively reviewed from the database. Of these, 106 patients with esophagogastric junctional cancer, which was defined as cancer with its epicenter within 5 cm of the junction and extending into the esophagus, were not included. In addition, 43 patients who had received neoadjuvant chemotherapy and 57 patients with stage IV cancer, including peritoneal seeding, positive peritoneal cytology, para-aortic lymph node metastases, and liver metastases were excluded. Wall-penetrating gastric cancer was defined as cancer with deeper wall invasion than the submucosa (≥stage T2); thus, 404 patients with T1 disease were excluded. Therefore, a total of 262 patients with wall-penetrating tumors were investigated. The demographic data of the patients were recorded.

Disease staging

The staging was conducted according to the International Union Against Cancer (UICC) TNM classification (7th edition) [23]. The T stage and nodal status were determined based on histopathological evaluation. The accuracy rate of preoperative diagnosis for T4 stage was 50.3%. The histological features of the resected specimens were also evaluated. Papillary and tubular adenocarcinomas were categorized as well differentiated, whereas poorly differentiated adenocarcinoma and signet ring cell carcinoma were classified into the poorly differentiated category.

Peripheral blood parameters

Routine venous blood samples were collected from the patients for preoperative determination of blood cell counts, laboratory parameters, and tumor markers. Samples from patients with evidence of infectious conditions were excluded. Blood samples were collected in ethylenediamine tetraacetic acid (EDTA)-containing tubes for blood cell counting, in tubes containing coagulation accelerators for determination of laboratory parameters, and in 3.13% sodium citrate-containing tubes for analysis of the coagulation profile. Blood cell counts and the coagulation profile were measured using an XE-2100™ Automated Hematology System and an CA-1500 System automated blood coagulation analyzer (Sysmex Co., Kobe, Japan), respectively. The laboratory parameters and serum levels of carcinoembryonic antigen (CEA) were estimated using a Automatic Analyzer model 7700 series (Hitachi High Technologies Co., Ltd., Tokyo, Japan). Serum levels of the carbohydrate antigen (CA) 19-9 were determined using a Full Random Access Immunoassay LUMIPULSE® system (Fujirebio, Inc., Tokyo, Japan). Hematologic values, including the white blood cell count (WBC), neutrophil count (Neu), lymphocyte count (Lym), monocyte count (Mono), and platelet count (Plt), and the laboratory data, including the serum hemoglobin (Hb) and albumin (Alb), prothrombin time (PT), C-reactive protein (CRP), activated partial thromboplastin time (APTT), and serum CEA and CA19-9 were retrospectively identified. Then, the neutrophil/lymphocyte ratio (NLR) was calculated by dividing the neutrophil count by the lymphocyte count.

Statistics

Data are presented as medians and ranges. The preoperative hematological and biochemical parameters were compared in relation to the T stage, nodal status, and histological features using the Kruskal–Wallis test and the Mann–Whitney U test. Receiver operating characteristic (ROC) curves were constructed in order to calculate the sensitivity, specificity, positive predictive value, and negative predictive value for T4 disease. Cutoff values for the NLR with the best combination of predictive values were chosen. First, the χ^2 and Fisher's exact tests were used for univariate comparison of each of the hematological parameters of interest. Variables found to be significant on univariate analysis were subjected to multivariate analysis by multiple logistic regression analysis. The significance level was set at $P < 0.05$. All statistical analyses were performed using SPSS II for Windows (SPSS Japan, Tokyo, Japan).

Results

Demographic characteristics

The median age of the 262 patients enrolled in the study at diagnosis was 64 years, all the patients were Asian, 180

(68.7%) were male, and 82 (31.3%) were female. The demographics and tumor-related factors are summarized in Table 1. The depth of invasion of the primary lesion was assessed as stage T4 in 61 (23.3%) patients. The number of patients with positive nodal status was 158 (60.3%). All of the patients underwent curative resection with systematic D2 lymph node dissection. In all, 41 (15.6%), 116 (44.3%), and 105 (40.1%) patients were classified as having stage I, stage II and stage III disease, respectively. The type of surgical intervention used was total gastrectomy in 84 (32.1%) patients, distal and proximal gastrectomy in 169 (64.5%) and 8 (3.1%) patients, respectively, and pancreatoduodenectomy in 1 (0.4%) patient. The histological features are given in Table 1. Of the 262 patients, 115 (43.9%) were classified into the well-differentiated tumor category and 143 (54.6%) into the poorly differentiated tumor category. Mucinous carcinoma was diagnosed in 4 (1.5%) patients. The median follow-up period of the surviving cases was 54.5 months, and 36 (13.7%) patients died within 5 years of surgery. The overall cumulative 3-year (3Y-OS) and 5-year (5Y-OS) survival rates were 87.8 and 82.9%, respectively.

Table 1 Demographics and tumor-related factors

Number	262
Male:female	180:82
Median age (range)	64 (30–92)
Histological features, *n* (%)	
Papillary	6 (2.0)
Tubular	109 (41.6)
Poorly differentiated	123 (46.9)
Signet ring cell	20 (7.6)
Mucinous	4 (1.5)
Pathological depth of penetration, *n* (%)	
T2	78 (29.8)
T3	123 (46.9)
T4	61 (23.3)
Pathological nodal status, *n* (%)	
N0	104 (39.7)
N1	53 (20.2)
N2	47 (17.9)
N3	58 (22.1)
TNM stage/pathological, *n* (%)	
Stage I	41 (15.6)
Stage II	116 (44.3)
Stage III	105 (40.1)

Demographics and tumor-related factors of 262 patients with ≥T2 gastric cancer who underwent surgical intervention at the NCCHE between 2002 and 2005 are displayed

Relationship between the peripheral blood parameters and tumor-related factors

In all 262 patients, the median levels of the all serum parameters were within the normal ranges. The data for each T stage were analyzed and are presented in Table 2. An increase in the NLR ($P = 0.004$) and CRP ($P = 0.017$) and a decrease in the Lym ($P = 0.032$), Hb ($P < 0.001$), and CEA ($P = 0.029$) in a T stage-dependent manner were observed. The data were also compared in relation to the nodal status and histological features of the tumors (data not shown). Patients with nodal positivity showed only decreased serum Hb and Alb levels compared to the patients with node-negative status. Poorly differentiated tumors were associated with decreased Mono and CEA.

Predictive significance of parameters for T4 tumor stage

The peripheral hematological parameters showed a greater degree of correlation with the T stage than with the nodal status or histological features. Thus, the predictive value of the parameters for T4 disease, which was defined as the presence of serosal invasion according to the UICC TNM classification [23], was assessed.

The ROC curves for the continuous variables of NLR constructed for predicting T4 disease are shown in Fig. 1. The area under the curve (AUC) was recorded as 0.605 (95% confidence interval [CI], 0.525–0.684) for the NLR. The sensitivity, specificity, positive predictive value, and negative predictive value of NLR >3.2 ($n = 103$) for predicting T4 disease were 55.7, 65.7, 33.0, and 83.0%, respectively. We defined high NLR according to the cutoff values mentioned above, which yielded the best combination of predictive values.

Next, the predictive value of the NLR was compared with those of the other parameters. Univariate and multivariate logistic regression analyses to determine the predictive factors for T4 disease were performed, as shown in Table 3. Significant differences in the odds ratio (OR) were observed for differential levels of Hb (OR = 2.020, 95% CI = 1.126–3.624; $P = 0.018$), NLR (OR = 2.036, 95% CI = 1.139–3.639; $P = 0.026$), CA19-9 (OR = 2.175, 95% CI = 1.020–4.640; $P = 0.044$), and poorly differentiated histology (OR = 3.061, 95% CI = 1.602–5.848; $P = 0.001$). According to multiple logistic regression analysis, Hb (OR = 1.875, 95% CI = 1.005–3.500; $P = 0.048$), NLR (OR = 2.206, 95% CI = 1.187–4.100; $P = 0.012$), and poorly differentiated histology (OR = 3.134, 95% CI = 1.593–6.167; $P = 0.001$) were identified as independent predictive factors for T4 disease.

Table 2 Baseline hematological values and laboratory data

Variables	T2	T3	T4	*P*
WBC (/μl)	5,950 (3,500–12,000)	6,100 (1,300–9,800)	6,100 (2,200–13,200)	0.742
Neu (/μl)	3,955 (1,760–9,350)	3,990 (530–7,720)	4,280 (1,190–10,790)	0.361
Lym (/μl)	1,585 (720–2,990)	1,380 (480–3,250)	1,410 (620–2,510)	0.032
Mono (/μl)	295 (100–550)	290 (60–800)	270 (110–620)	0.202
Hb (g/dl)	13.65 (6.7–16.5)	12.8 (5.5–16.5)	12.3 (6.0–16.3)	<0.001
Plt ($\times 10^4$/μl)	24.45 (9.7–41.4)	27.3 (8.0–51.2)	26.4 (15.3–56.5)	0.146
NLR	2.568 (0.863–5.927)	2.788 (0.898–13.542)	3.322 (1.311–9.695)	0.004
CRP (mg/dl)	0.1 (0–6.1)	0.1 (0–5.7)	0.1 (0–10.4)	0.017
Alb (g/dl)	4.2 (3.2–4.8)	4.1 (2.6–4.7)	4.0 (2.7–4.6)	0.063
PT (s)	11.4 (10.5–12.7)	11.5 (10.0–13.0)	11.4 (10.4–12.8)	0.07
APTT (s)	26.8 (21–38)	26.3 (21.0–40.0)	28.1 (21.0–43.0)	0.067
CEA (ng/ml)	2.9 (0.6–32.8)	2.9 (0.6–187)	2.1 (0.6–155.2)	0.029
CA19-9 (U/ml)	12 (1–139)	12.5 (0.1–412)	14.0 (0.1–633)	0.354

Values are median (range). Data for each T stage are shown. The significance was evaluated using the Kruskal–Wallis test

Neu neutrophil count, *Lym* lymphocyte count, *Mono* monocyte count, *NLR* neutrophil/lymphocyte ratio

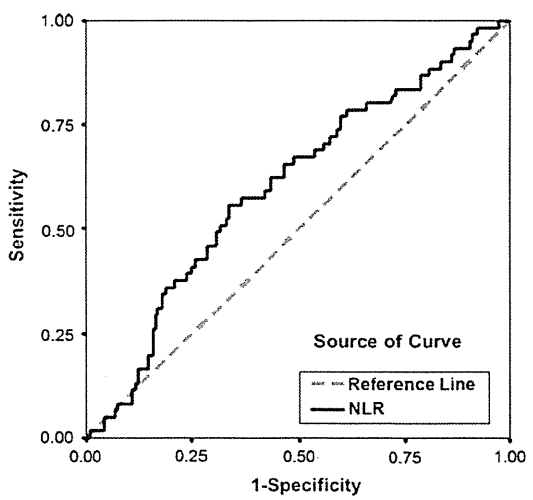

Fig. 1 ROC curve to assess the predictive value of the NLR in determining the T4 stage is shown

Discussion

Blood samples were easily assessable and reliable factors for preoperative prediction. In particular, NLR has been reported to be a prognostic factor in gastric cancer patients [15, 17, 20–22]. We analyzed the relationship between NLR and tumor-related factors in patients with wall-penetrating gastric cancer, for whom we sometimes need to consider neoadjuvant therapies. A large phase III trial demonstrated the efficacy of neoadjuvant chemotherapy in similar patients who were estimated to be stage II or higher with neither distant metastases nor locally advanced inoperable disease [5]. In the present study, NLR was correlated with T stage rather than with the nodal status or the histological features. The result suggested that the tissue damage and remodeling around invasive tumors had an effect on the systemic inflammatory response. The prognostic value of NLR in gastric cancer might depend on the T stage.

Neutrophils represent early acute inflammation and migrate to the affected sites to neutralize and eliminate potentially injurious stimuli [24]. Increased neutrophil counts have been observed in patients with gastric cancer [25]. Likewise, the production of tumor-promoting inflammatory chemokines and cytokines has been shown to trigger the recruitment of myeloid cells to most tumors related to inflammation, and gastric cancer cells overexpress C-X-C motif chemokine ligand 8 (CXCL8, known as IL-8), which induces migration of the chemokine receptor CXCR1 (also known as IL-8 receptor α) expressed on neutrophils across the tumor site [25]. Recruited neutrophils, along with the tumor-associated macrophages (TAM), have been shown to be a major source of matrix metalloproteinase 9 (MMP9) in various murine tumor models [26]. The prior partial degradation of the extracellular matrix by MMPs allows cell infiltration into the tissue [27]; in addition, vascular endothelial growth factor A (VEGF-A), derived from TAM, mediates endothelial cell mitogenesis and vascular permeability [28]. The present study demonstrated a T-stage-dependent increase in the neutrophil count in the peripheral blood (Table 2), reflecting recruitment of neutrophils from the bone marrow to the tumor site; however, no statistically significant differences were observed.

The lymphocytopenia was presumably a part of an immune-tolerated microenvironment around the tumor and has been suggested as an independent prognostic factor in

Table 3 Univariate and multivariate logistic regression analyses to determine the risk of stage T4

Variables	*n*	Univariate analysis		Multivariate analysis		
		OR (95% CI)	*P*	OR (95% CI)	*B*	*P*
Lym <1,000 (/μl)	41	1.673 (0.805–3.477)	0.168	–	–	–
Hb <13.0 (g/dl)	121	2.020 (1.126–3.624)	0.018	1.875 (1.005–3.500)	0.639	0.048
Plt >25.0 ($\times 10^4$/μl)	142	1.291 (0.722–2.306)	0.389	–	–	–
CRP >1 (mg/dl)	20	2.377 (0.924–6.117)	0.072	–	–	–
NLR >3.2	103	2.036 (1.139–3.639)	0.016	2.206 (1.187–4.100)	0.783	0.012
Alb <3.5 (g/dl)	24	2.146 (0.889–5.183)	0.090	–	–	–
PT >median	99	0.777 (0.403–1.403)	0.403	–	–	–
APTT >median	133	1.846 (0.990–3.442)	0.054	–	–	–
CEA >5 (ng/ml)	47	0.826 (0.384–1.773)	0.623	–	–	–
CA19-9 >37 (U/ml)	35	2.175 (1.020–4.640)	0.044	2.073 (0.918–4.679)	0.718	0.079
Poorly differentiated	143	3.061 (1.602–5.848)	0.001	3.134 (1.593–6.167)	1.144	0.001

The significance in univariate analysis was evaluated using χ^2 and Fisher's exact tests. The significance in multivariate analysis was evaluated using multiple logistic regression analysis. The regression coefficient *B* is also given

several cancers [18]. Interestingly, a significant decrease in the lymphocyte count was also observed in a T-stage-dependent manner (Table 2). This result indicated the possibility that neutrophil-induced tissue damage and remodeling around the tumor site contributed to the establishment of the host's adaptive immunity.

T4 disease has newly been defined in the 7th edition of the UICC TNM classification as a tumor perforating the serosa or invading adjacent structures [23], and includes remodeling through all the gastric layers. In cases with T4 disease, the neutrophil counts reached their peak, while the lymphocyte counts reached their nadir, yielding the maximum NLR (Table 2). An earlier study also reported a consistent T-stage-dependent increase in NLR in gastric cancer [20]. Furthermore, a high NLR, defined as >3.2 in the present study, was an independent predictor of T4 disease according to multiple logistic regression analysis, as was a decrease in the Hb and poorly differentiated tumor histology. Anemia presumably reflected the blood loss at the tumor site. CA19-9 was correlated with the T stage but was not an independent predictive factor for T4 disease. The histological differentiation grade was the most reliable risk factor, but the histology of biopsy samples obtained through endoscopic examination did not always match that of the corresponding resected specimens. Although serum CRP and Alb have been previously suggested as inflammation-based prognostic factors in advanced cancers [16, 29, 30], both were not meaningful predictive factors for T4 disease. Therefore, the high baseline of NLR was suggested as a valuable predictive factor for T4 disease, and its predictive value was superior to serum tumor markers.

The clinical diagnostic accuracy rate for T4 disease was 50.3% in the present study. This low accuracy rate was attributable to the conventional axial CT images without gastric water filling or radiological examinations. Actually, it was known that the clinical TNM staging of gastric cancer before treatment was not in accord with pathological staging in a substantial number of cases. Recently, the accuracy of preoperative staging of gastric cancer was improved by MDCT with multiplanar reconstruction (MPR) images. The diagnostic accuracy of MDCT for T4 disease was reported to be up to 93% [8–11], and a prospective study to confirm the reproducibility in a larger sample is awaited. Though the NLR seems to add valuable preoperative information to clinical TNM staging, the utility of NLR still requires the comparison with novel imaging modalities like MDCT before the introduction into clinical practice.

In conclusion, we found NLR as an independent predictive factor for T4 disease to be superior to other serum factors. The clinical utility of NLR still needs to be confirmed with prospective analysis.

Disclosure The authors have no conflicts of interest or financial ties to disclose.

References

1. Jemal A, Siegel R, Ward E et al (2009) Cancer statistics, 2009. CA Cancer J Clin 59:225–249
2. Noguchi Y, Yoshikawa T, Tsuburaya A et al (2000) Is gastric carcinoma different between Japan and the United States? Cancer 89:2237–2246
3. Maruyama K, Okabayashi K, Kinoshita T (1987) Progress in gastric cancer surgery in Japan and its limits of radicality. World J Surg 11:418–425. doi:10.1007/BF01655804
4. Sakuramoto S, Sasako M, Yamaguchi T et al (2007) Adjuvant chemotherapy for gastric cancer with S-1, an oral fluoropyrimidine. N Engl J Med 357:1810–1820

5. Cunningham D, Allum WH, Stenning SP et al (2006) Perioperative chemotherapy versus surgery alone for resectable gastroesophageal cancer. N Engl J Med 355:11–20
6. Macdonald JS, Smalley SR, Benedetti J et al (2001) Chemoradiotherapy after surgery compared with surgery alone for adenocarcinoma of the stomach or gastroesophageal junction. N Engl J Med 345:725–730
7. Brennan MF (2005) Current status of surgery for gastric cancer: a review. Gastric Cancer 8:64–70
8. Chen CY, Hsu JS, Wu DC et al (2007) Gastric cancer: preoperative local staging with 3D multi-detector row CT—correlation with surgical and histopathologic results. Radiology 242:472–482
9. Habermann CR, Weiss F, Riecken R et al (2004) Preoperative staging of gastric adenocarcinoma: comparison of helical CT and endoscopic US. Radiology 230:465–471
10. Hwang SW, Lee DH, Lee SH et al (2010) Preoperative staging of gastric cancer by endoscopic ultrasonography and multidetector-row computed tomography. J Gastroenterol Hepatol 25:512–518
11. Kumano S, Murakami T, Kim T et al (2005) T staging of gastric cancer: role of multi-detector row CT. Radiology 237:961–966
12. de Graaf GW, Ayantunde AA, Parsons SL et al (2007) The role of staging laparoscopy in oesophagogastric cancers. Eur J Surg Oncol 33:988–992
13. Coussens LM, Werb Z (2002) Inflammation and cancer. Nature 420:860–867
14. Mantovani A, Allavena P, Sica A et al (2008) Cancer-related inflammation. Nature 454:436–444
15. Aliustaoglu M, Bilici A, Ustaalioglu BB et al (2010) The effect of peripheral blood values on prognosis of patients with locally advanced gastric cancer before treatment. Med Oncol 27(4): 1060–1065
16. Crumley AB, McMillan DC, McKernan M et al (2006) An elevated C-reactive protein concentration, prior to surgery, predicts poor cancer-specific survival in patients undergoing resection for gastro-oesophageal cancer. Br J Cancer 94:1568–1571
17. Mohri Y, Tanaka K, Ohi M et al (2010) Prognostic significance of host- and tumor-related factors in patients with gastric cancer. World J Surg 34:285–290. doi:10.1007/s00268-009-0302-1
18. Ray-Coquard I, Cropet C, Van Glabbeke M et al (2009) Lymphopenia as a prognostic factor for overall survival in advanced carcinomas, sarcomas, and lymphomas. Cancer Res 69: 5383–5391
19. Satomi A, Murakami S, Ishida K et al (1995) Significance of increased neutrophils in patients with advanced colorectal cancer. Acta Oncol 34:69–73
20. Shimada H, Takiguchi N, Kainuma O et al (2010) High preoperative neutrophil-lymphocyte ratio predicts poor survival in patients with gastric cancer. Gastric Cancer 13:170–176
21. Ubukata H, Motohashi G, Tabuchi T et al (2010) Evaluations of interferon-gamma/interleukin-4 ratio and neutrophil/lymphocyte ratio as prognostic indicators in gastric cancer patients. J Surg Oncol 102(7):742–747
22. Yamanaka T, Matsumoto S, Teramukai S et al (2007) The baseline ratio of neutrophils to lymphocytes is associated with patient prognosis in advanced gastric cancer. Oncology 73: 215–220
23. Sobin LH, Wittekind C (eds) (2010) TMN Classification of Malignant Tumours (UICC). Wiley-Blackwell, Chichester, UK
24. Serhan CN, Brain SD, Buckley CD et al (2007) Resolution of inflammation: state of the art, definitions and terms. FASEB J 21:325–332
25. Eck M, Schmausser B, Scheller K et al (2003) Pleiotropic effects of CXC chemokines in gastric carcinoma: differences in CXCL8 and CXCL1 expression between diffuse and intestinal types of gastric carcinoma. Clin Exp Immunol 134:508–515
26. Coussens LM, Tinkle CL, Hanahan D et al (2000) MMP-9 supplied by bone marrow-derived cells contributes to skin carcinogenesis. Cell 103:481–490
27. Kido S, Kitadai Y, Hattori N et al (2001) Interleukin 8 and vascular endothelial growth factor—prognostic factors in human gastric carcinomas? Eur J Cancer 37:1482–1487
28. Yancopoulos GD, Davis S, Gale NW et al (2000) Vascular-specific growth factors and blood vessel formation. Nature 407:242–248
29. Crumley AB, Stuart RC, McKernan M et al (2008) Comparison of an inflammation-based prognostic score (GPS) with performance status (ECOG-ps) in patients receiving palliative chemotherapy for gastroesophageal cancer. J Gastroenterol Hepatol 23:e325–e329
30. McMillan DC (2008) An inflammation-based prognostic score and its role in the nutrition-based management of patients with cancer. Proc Nutr Soc 67:257–262

Application of activity pencil beam algorithm using measured distribution data of positron emitter nuclei for therapeutic SOBP proton beam

Aya Miyatake[a)]
Keen Medical Physics Co. Ltd., 901-4-4-4 Yushima, Bunkyo-ku, Tokyo 113-0034, Japan

Teiji Nishio
Particle Therapy Division, Research Center for Innovative Oncology, National Cancer Center, Kashiwa, 6-5-1 Kashiwano-ha, Kashiwa-shi, Chiba 277-8577, Japan

(Received 9 October 2012; revised 24 July 2013; accepted for publication 29 July 2013; published 16 August 2013)

Purpose: Recently, much research on imaging the clinical proton-irradiated volume using positron emitter nuclei based on target nuclear fragment reaction has been carried out. The purpose of this study is to develop an activity pencil beam (APB) algorithm for a simulation system for proton-activated positron-emitting imaging in clinical proton therapy using spread-out Bragg peak (SOBP) beams.

Methods: The target nuclei of activity distribution calculations are ^{12}C nuclei, ^{16}O nuclei, and ^{40}Ca nuclei, which are the main elements in a human body. Depth activity distributions with SOBP beam irradiations were obtained from the material information of ridge filter (RF) and depth activity distributions of compounds of the three target nuclei measured by BOLPs-RGp (beam ON-LINE PET system mounted on a rotating gantry port) with mono-energetic Bragg peak (MONO) beam irradiations. The calculated data of depth activity distributions with SOBP beam irradiations were sorted in terms of kind of nucleus, energy of proton beam, SOBP width, and thickness of fine degrader (FD), which were verified. The calculated depth activity distributions with SOBP beam irradiations were compared with the measured ones. APB kernels were made from the calculated depth activity distributions with SOBP beam irradiations to construct a simulation system using the APB algorithm for SOBP beams.

Results: The depth activity distributions were prepared using the material information of RF and the measured depth activity distributions with MONO beam irradiations for clinical therapy using SOBP beams. With the SOBP width widening, the distal fall-offs of depth activity distributions and the difference from the depth dose distributions were large. The shapes of the calculated depth activity distributions nearly agreed with those of the measured ones upon comparison between the two. The APB kernels of SOBP beams were prepared by making use of the data on depth activity distributions with SOBP beam irradiations that were made from the depth activity distributions with MONO beam irradiations and sorted in terms of energy, SOBP width, and thickness of FD. The data on APB kernels of SOBP beams were determined as installment data for the simulation system using the APB algorithm for SOBP beam irradiations.

Conclusions: A method of obtaining the depth activity distributions and the APB algorithm for clinical use of SOBP beams have been developed. It is suggested that the simulation system for imaging the clinical irradiated volume with the APB algorithm can be used in clinical proton therapy using SOBP beams by preparing and investigating the data on APB kernels of SOBP beams.
© *2013 American Association of Physicists in Medicine.* [http://dx.doi.org/10.1118/1.4818057]

Key words: proton therapy, SOBP beam, imaging the clinical proton-irradiated volume, simulation of activity distribution, activity pencil beam algorithm, beam ON-LINE PET system, target nuclear fragment reaction

1. INTRODUCTION

Proton therapy is a form of radiotherapy that can be concentrated on a tumor using a scanned or modulated Bragg peak. To use this radiotherapy efficiently in a clinical context, it is necessary to evaluate the clinical proton-irradiated volume accurately. Therefore, proton therapy has been performed for patients with measurement using the Beam ON-LINE PET system mounted on a rotating gantry port (BOLPs-RGp) at the National Cancer Center, Kashiwa (NCCE), since October 2007 (Ref. 1). BOLPs-RGp was installed in a treatment room with the dual-ring double scattering method.[2,3] Some clinical analyses of clinical proton-irradiated volume were reported by verifying the patient data measured by BOLPs-RGp.[1,4]

Human body is mostly composed of five elements: H, C, N, O, and Ca. It is known that reaction cross section of ^{14}N(p, α)^{11} C reaction is over 200 mb only around proton beam range (just before a beam stop)[5]. ^{11}C nuclei have a long half-life time of about 20 min. However, activity distributions are formed mainly by information of ^{15}O nuclei with short

half-life about 2 min because measurement time is several minutes at the most in a clinical case using online PET. In addition, compositional rate of N nuclei are smaller than H, C, O, and Ca nuclei in target organs for proton therapy (the rate of N: $\sim$ 2.7%).[6] Therefore, it is thought that existence of N nuclei can be ignored in the clinical case using BOLPs-RGp. In case it needs time interval between the end of proton irradiation and the start of PET measurement such as offline PET, it may be necessary to consider existence of N nuclei because ^{11}C and ^{13}N (half-life about 10 min) with long half-life nuclei are main information for activity distributions. Consequently, important nuclei for imaging the clinical proton-irradiated volume in a patient's body are positron emitter nuclei of ^{11}C, ^{10}C, ^{15}O, ^{14}O, and ^{38}K, etc., generated by target nuclear fragment reaction of ^{12}C, ^{16}O, and ^{40}Ca nuclei with proton of therapeutic beam energy for proton therapy. A calculation algorithm, activity pencil beam (APB) algorithm, that has both sufficient accuracy and useful calculation time in clinical proton therapy for a simulation system of proton-activated positron-emitting imaging was developed and proposed.[7] The simulation system has some important functions: import function of CT image data, ROI information, a result data of calculated dose distributions in DICOM-RT Ion format and original formatted activity distribution data measured by BOLPs-RGp, calculation function of activity distributions using APB algorithm and verification function of comparison among calculated dose distributions, measured activity distributions and calculated activity distributions. For proton therapy with high accuracy, it is important to construct a simulation system for imaging the clinical proton-irradiated volume in clinical use. A lot of reports on phantom studies, simulation studies, patients studies and so on for proton therapy have been published.[1,4,7–21]

Some hospitals and facilities use pencil beam scanning for proton therapy and others use broad beam as spread-out Bragg peak (SOBP) beam. SOBP for the uniform dose distribution in the depth direction is the sum of several Bragg peaks made by a proton beam passing through bar-ridge filter (RF) or range modulators at staggered depths. In a facility using RF, a filter is designed in consideration of scattering and nuclear interaction effect within the filter itself to produce a three-dimensionally uniform SOBP.[22] In the simulation system discussed in our previous report, activity distribution is calculated using APB algorithm with APB kernels prepared by the data of mono-energetic (MONO) beam irradiations.[7] If an activity distribution with SOBP beam irradiation is calculated using the previous method, the required number of calculation sets is equal to the number of beams forming the SOBP. Furthermore, it needs enormous time to measure data for APB kernels that users should prepare for the simulation system using APB algorithm. These are reason for difficulty of the use of method reported in our previous report, because short calculation time and user-friendly system were required in a clinical radiotherapy context.

In our early publication, a calculated APB kernel for a MONO beam consists a magnitude based on measured positron-emitting activity along the depth and a Gaussian function for mimicking the effect of multiple Coulomb scattering.[5] The magnitude is characterized by the contributions of long and short half-life components. Based on calculated mono-energetic APB kernel without re-establishing parameters for the depth or lateral profile, a simple sum of contributions of each energy layer of mono-energetic protons for forming modulated proton (i.e., SOBP) can be performed.

In this paper, to make it possible to simulate an activity distribution with SOBP beam irradiation using APB algorithm, we establish making APB kernels with SOBP beam irradiation using measured depth activity distribution with MONO beam irradiation and the material information of RF. It becomes to propose an application of APB algorithm for proton therapy of SOBP beams.

2. MATERIALS AND METHODS

2.A. Clinical SOBP beam for proton therapy at NCCE

The dual-ring double scattering method has been used in the treatment room where BOLPs-RGp was installed at NCCE. After a proton beam passes through the dual-ring double scatters to produce a flat irradiation field in the lateral direction, it passes through an aluminum RF to produce a flat irradiation field in the depth direction.[3] RF prepared in our center allows us to select SOBP width from among eight grades between 30 and 100 mm in 10-mm steps.[3] Proton beam energies of 223, 179, and 138 MeV become those of 200, 159, and 121 MeV after a proton beam passes through the dual-ring double scatters. Proton ranges of 200, 159, and 121 MeV in the dual-ring double scattering system were shorter than those of 223, 179, and 138 MeV by 53.8, 39.6, and 27.7 mm, respectively.

Dose distributions were measured at intervals of 1 mm using a three-dimensional water phantom with a plane parallel ion chamber. The dose distributions at beam energies of 200, 159, and 121 MeV were measured with parameters of SOBP width and thickness of fine degrader (FD). FD is made of Lucite and used to adjust beam ranges. SOBP width was changed from 30 to 100 mm in 10-mm steps and the thickness of FD from 0 mm to the maximum thickness of 80 mm in the same steps. The maximum thickness of FD depends on beam energy and SOBP width. Percentage depth dose (PDD) was measured using the parallel ion chamber which was set at the position where isocenter was on the surface of the water. Distance from isocenter to FD is 989 mm and from isocenter to RF is 1696 mm. The water equivalent length of 1 cm FD (Lucite) is 1.16 cm by a preliminary experiment.

2.B. Calculation of depth activity distributions of clinical SOBP beam from measured depth activity distributions of MONO beam and material information of RF

SOBP is the sum of several beams (i beams) that a MONO beam is divided into by passing through RF. SOBP can be expressed using proton beam energy, material information of RF and the effect of multiple Coulomb scattering by RF and

FD such as the following Eq. (1),

$$\mathrm{SOBPd(E, RF, FD, z)} = \sum_{k}^{i}\{rf_k(\mathrm{E, RF}).fd_k(\mathrm{E, FD}) \cdot \mathrm{monod}_k(\mathrm{E, FD} = 0, \mathrm{z})\}. \quad (1)$$

Here, SOBPd denotes depth dose distribution with SOBP beam irradiation. SOBPd is a function with four parameters: incident proton energy, E, the information of RF and FD, RF and FD, and depth, z. Function of *rf* considers effect of energy loss, multiple Coulomb scattering and the number of protons caused by the information of RF. Function of *fd* also considers the scattering effect caused by thickness of FD. The monod denotes a depth-dose distribution measured in the case of MONO beam irradiation with incident proton energy E and FD = 0. You can replace depth-dose distribution with depth activity distribution with applying Eqs. (2) to (1),

$$\mathrm{SOBPd(E, RF, FD, z)} \rightarrow \mathrm{SOBPa(M, E, RF, FD, z)}$$
$$\mathrm{monod}_k(\mathrm{E, FD} = 0) \rightarrow \mathrm{monoa}_k(\mathrm{M, E, FD} = 0). \quad (2)$$

Here, SOBPa denotes depth activity distribution with SOBP beam irradiation. M denotes kind of target nucleus. The monoa denotes a depth activity distribution measured in the case of MONO beam irradiation. Depth activity distributions of SOBP beam (SOBP_act) can be calculated from measured depth activity distribution of MONO beam (MONO_act), material information of RF and FD thickness using Eqs. (1) and (2). In this study, the measured activity distributions of virtual positron emitter nuclei ($^{12}C_{virtual}$, $^{16}O_{virtual}$, and $^{40}C_{avirtual}$) reported in our previous study were used as the monoa (M = $^{12}C_{virtual}$, $^{16}O_{virtual}$, $^{40}Ca_{virtual}$; E = 121, 159, and 200 [MeV], FD = 0).[7] The virtual positron emitter nucleus was defined as the nuclei merged for various positron emitter nuclei generated from each target nucleus by target nuclear fragment reaction with proton beam irradiation.

Data of SOBP_act were prepared at three energies (121, 159, and 200 MeV), SOBP width for eight grades between 30 and 100 mm in 10-mm steps and the thickness of FD for nine levels between 0 and 80 mm in 10-mm steps.

2.C. Making of APB kernels for simulation of depth activity distributions using SOBP beam irradiations

If a calculation is performed using the method of simulation reported by Miyatake *et al.* (2011), it takes more time to calculate activity distributions with SOBP beam irradiations than MONO beam irradiations.[7] For example, to obtain a SOBP50 beam, a MONO beam is divided into 12 beams with different energies by passing through RF. Using the method reported by Miyatake *et al.* (2011) and the APB algorithm, SOBP_act is obtained by summing each calculated depth activity distribution made from 12 beams. Therefore, the calculation time required for simulating SOBP_act is 12 times that of MONO_act.

To shorten the calculation time, we propose a method which the APB kernels obtained by SOBP beam irradiations is prepared in advance. The APB algorithm which is a new method using APB kernels with SOBP beam irradiations can calculate SOBP_act with short time.

APB kernels were made from calculated SOBP_act based on measured MONO_act (see Sec. 2) and consideration of the effect of multiple Coulomb scattering, which was included in the lateral activity distributions with Gaussian form similar to proton dose calculation by pencil beam algorithm. The formula proposed by Lynch was used for the APB kernels in this study.[23] They were sorted by every clinical condition of SOBP beam (energy, SOBP width, and FD thickness).

3. RESULTS AND DISCUSSION

3.A. A Measured depth dose distributions of clinical SOBP beams at NCCE

Figure 1(a) is the measured depth dose distribution of each SOBP width at proton energy of 121, 159, and 200 MeV with FD = 0 mm. Figure 2(a) is the measured depth dose distribution of each FD thickness at proton energy of 121, 159, and 200 MeV with SOBP = 50 mm. All data of measured depth dose distributions of clinical SOBP beams were normalized at dose of SOBP center. The flatness of depth dose distribution in SOBP width was almost within ±1.5%. Dose at beam-entrance point in the SOBP width tends to fall by increase of FD thickness. It was observed that the measured beam ranges shifted regularly with a change of thickness of FD.

3.B. Comparison between calculated activity distributions and measured ones with SOBP beam irradiations

Figure 3 shows the calculated SOBP_act and the measured one around a range. The conditions of the irradiated proton beam were SOBP50-FD0 at 200 MeV. Comparing these distributions, an agreement within ±10% was observed. If we measure all of the data regarding SOBP_act to install a simulation system for imaging the clinical proton-irradiated volume, the measurement has to be carried out in each irradiation condition of three energies, eight SOBP widths and variable FD thickness. The total measurement time for all measurements is so enormous that preparation of all the data from the measurements is not feasible. Therefore, it was decided that the essential data to install the simulation system were to be obtained by calculating from the measured MONO_act and the material information of RF in our study.

3.C. Verification of the shape of calculated SOBP_act based on modulation of the measured MONO_act

Figures 1(b)–1(d) show measured MONO_act and the SOBP_act that were calculated from the MONO_act and the material information of RF. Activity distributions were normalized with each maximum value. Polyethylene, water, and calcium oxide were used as irradiation targets to measure activity distributions of positron emitter nuclei (^{11}C, ^{10}C, ^{15}O, ^{14}O, and ^{38}K, etc.) generated from three target nuclei (^{12}C, ^{16}O, and ^{40}Ca) in our previous study. Scaling factors

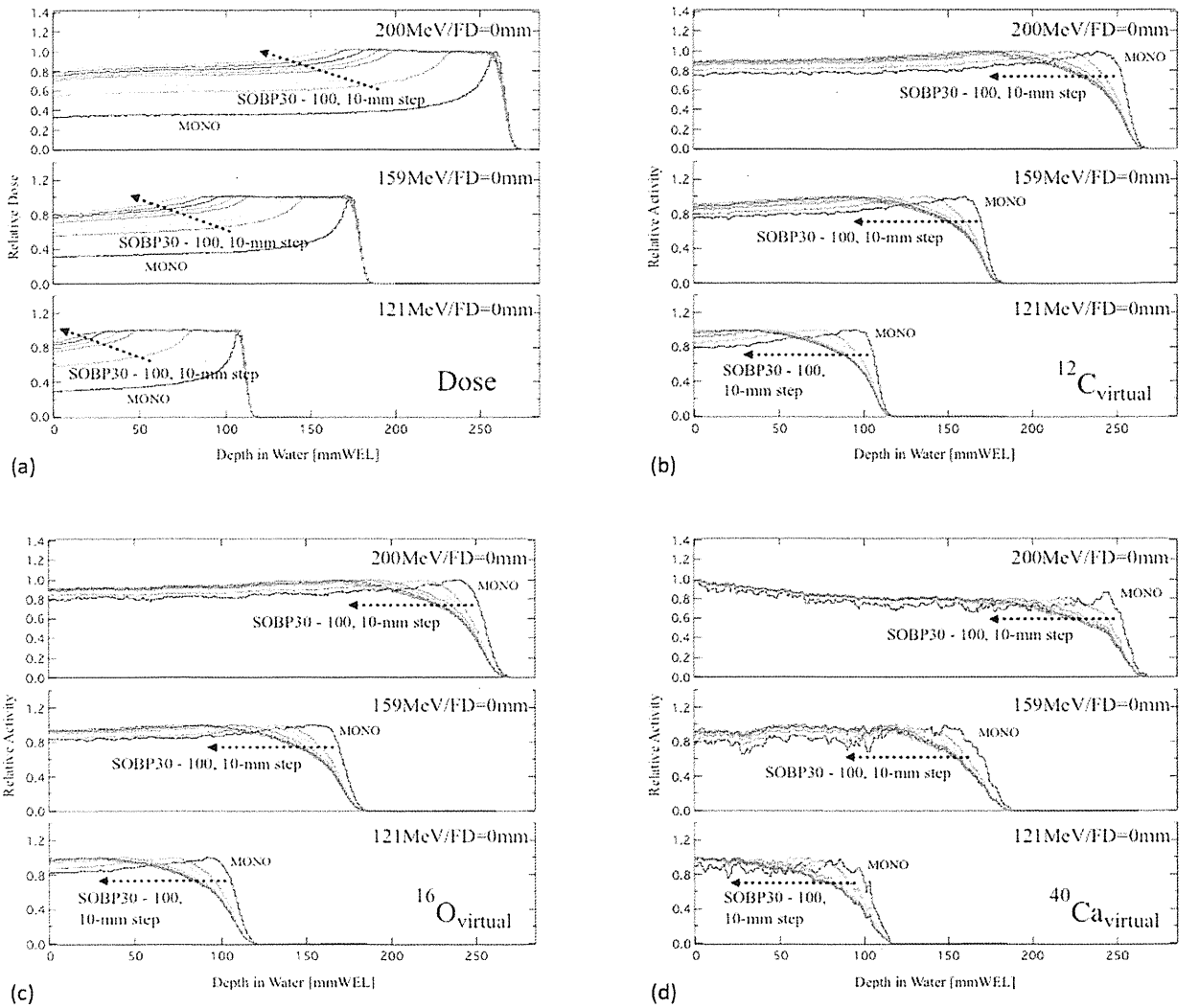

FIG. 1. (a) Measured depth dose distributions of MONO beams and SOBP beams, (b)–(d) Depth activity distributions of $^{12}C_{virtual}$, $^{16}O_{virtual}$, and $^{40}Ca_{virtual}$ in the case of SOBP beam irradiations. MONO activity distributions shown in (b)–(d) were measured. SOBP-depth activity distributions were calculated by modulation of measured MONO-depth activity distributions based on the material information of RF. The conditions of beam were FD = 0, SOBP widths from 30 to 100 mm with 10-mm steps at energies of 121, 159, and 200 MeV.

of polyethylene and calcium oxide against water calculated by measurement of beam range using proton beam.[7] It was observed that distal fall-off of the calculated SOBP_act and the differences in shapes between depth dose distributions and SOBP_act were wider with increasing SOBP width. The activity range (R_{act}), which is defined as a depth point whose relative activity value is 50%-value in SOBP-center normalized, was analyzed to verify a change of range position in SOBP_act and the result at 159 MeV is shown in Fig. 4. Although there were few changes in range positions in dose distributions with the parameter of SOBP width under constant FD thickness, R_{act} were shifted with SOBP width regularly in SOBP_act of $^{12}C_{virtual}$ and $^{16}O_{virtual}$. It is proved that ranges in SOBP_act were influenced by SOBP width and the kind of nucleus.

Calculated depth activity distributions of each kind of virtual nucleus with the parameter of FD thickness and constant SOBP50 and measured MONO_act are shown in Figs. 2(b)–2(d). Dose distributions almost kept their shapes and positions of ranges were shifted regularly with changes of FD thickness. In SOBP_act of three virtual nuclei, shapes changed more as FD thickness increased and ranges were shifted gradually with changes of FD thickness. It was found that shapes of SOBP_act were different for the three virtual nuclei and beam energies. Variations of R_{act} were analyzed about SOBP_act of each virtual nucleus with changing SOBP width and FD thickness. The result of analysis with a 159-MeV proton beam is shown in Fig. 5. It is illustrated that there was a linear relationship between range in SOBP_act and FD thickness within ±5% accuracy in each virtual nucleus regardless of changing SOBP width. Although the shapes of SOBP_act were influenced by FD thickness, the linear relationship was seen clearly. Therefore, we suppose that R_{act} can be estimated using the relationship with FD thickness. In addition, R_{act} can be

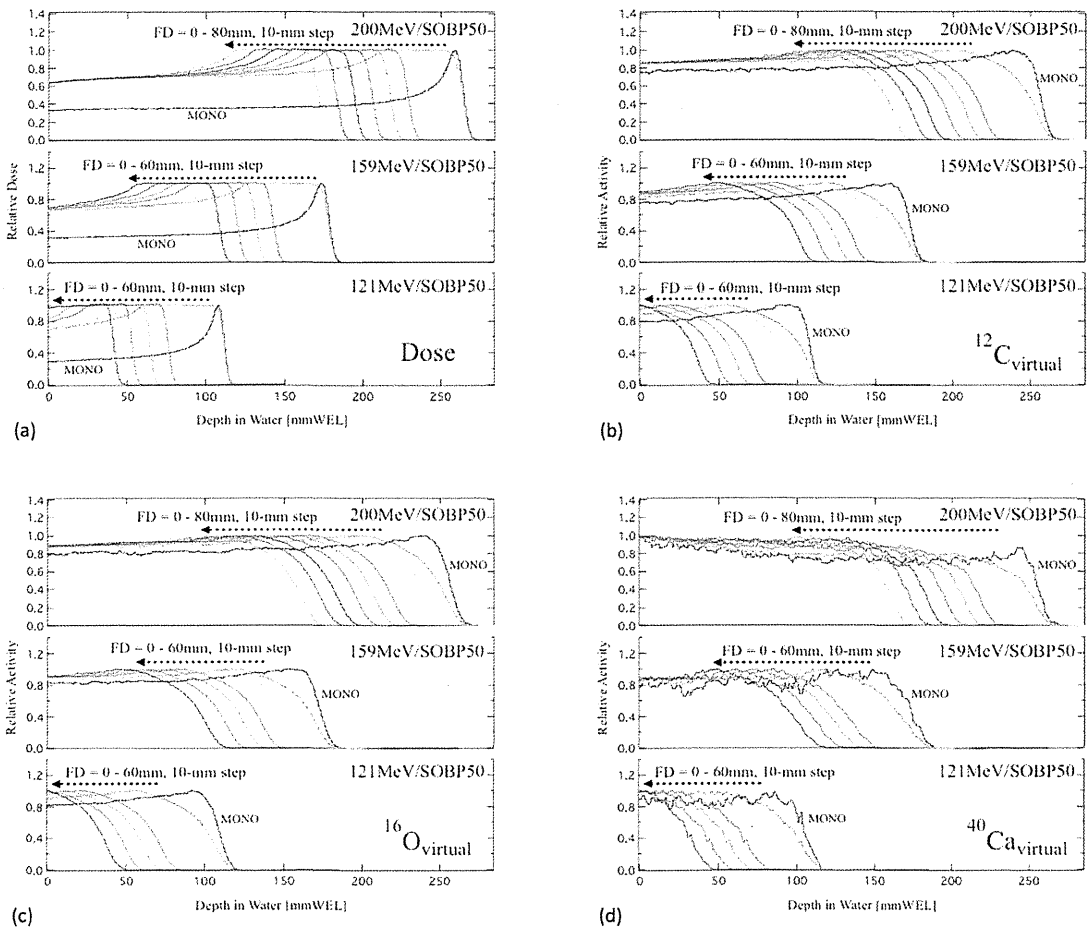

FIG. 2. (a) Measured depth dose distributions of MONO beams and SOBP beams, (b)–(d) Calculated depth activity distributions of $^{12}C_{virtual}$, $^{16}O_{virtual}$, and $^{40}Ca_{virtual}$ in the case of SOBP50 beam irradiations. MONO activity distributions shown in (b)–(d) were measured. SOBP-depth activity distributions were calculated by modulation of measured MONO-depth activity distributions based on the material information of RF. Proton beam energies were 121, 159, and 200 MeV. The thickness of FD was changed from 0 to 60 or 80 mm depending on beam energy.

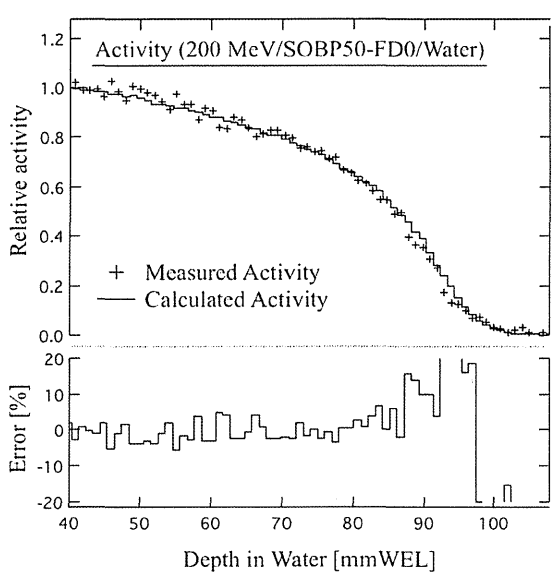

FIG. 3. Measured SOBP_act and calculated SOBP_act around a range with SOBP50-FD0 beam irradiation at 200 MeV in water. The shown error was calculated by defining the measured value as true.

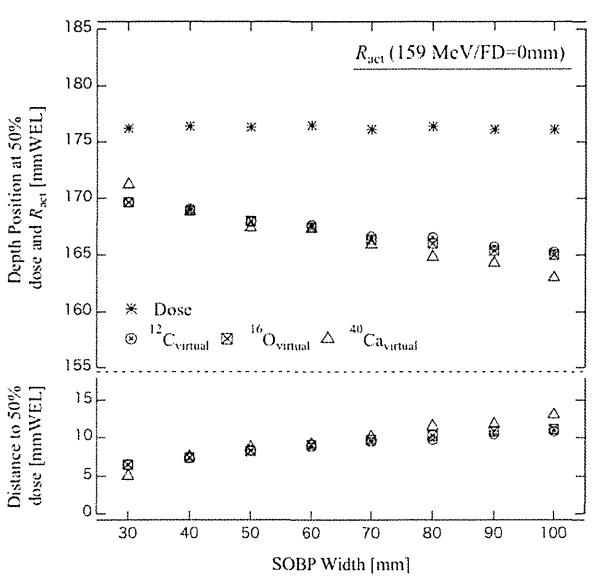

FIG. 4. Relationship between R_{act} and SOBP width in SOBP_act of each kind of virtual positron emitter nucleus in the beam irradiation condition of 159 MeV and FD = 0.

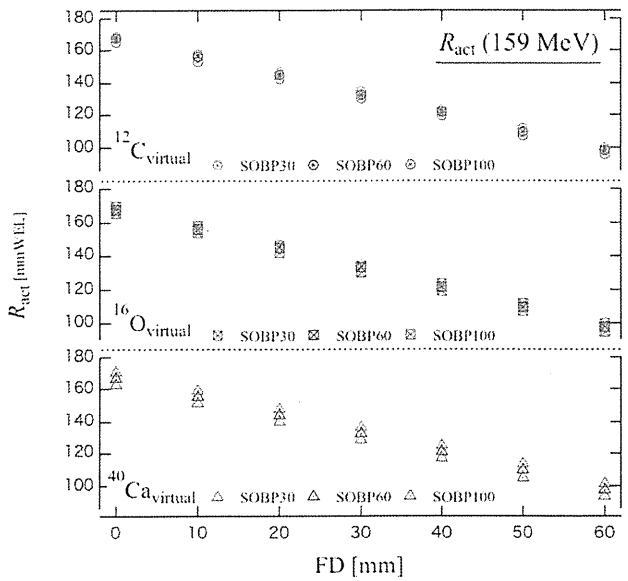

FIG. 5. Change of R_{act} with the parameter of FD thickness in SOBP_act of $^{12}C_{virtual}$, $^{16}O_{virtual}$, and $^{40}Ca_{virtual}$. The conditions of irradiated proton beam were SOBP30, SOBP60, and SOBP100 at 159 MeV.

expected to be an important parameter to estimate the range of dose distribution.

3.D. SOBP APB kernels for clinical proton therapy

APB kernels constructed by the calculated SOBP_act were prepared for simulation of imaging the clinical protonirradiated volume using the APB algorithm. The kernels of $^{12}C_{virtual}$, $^{16}O_{virtual}$, and $^{40}Ca_{virtual}$ were made in every irradiation condition of energy, SOBP width and FD thickness in our center. As an example of the kernels, depth or lateral activity (or dose) distributions and depth activity (or dose) distributions at a lateral point from the center axis by 1-mm steps are shown in Fig. 6. Dose distributions were measured and calculated in water.

3.E. Verification of a slope of SOBP between measured depth dose distributions and calculated activity distributions

SOBP has a slight slope of lower dose in the beam incident side with FD being thicker because the scatter of the

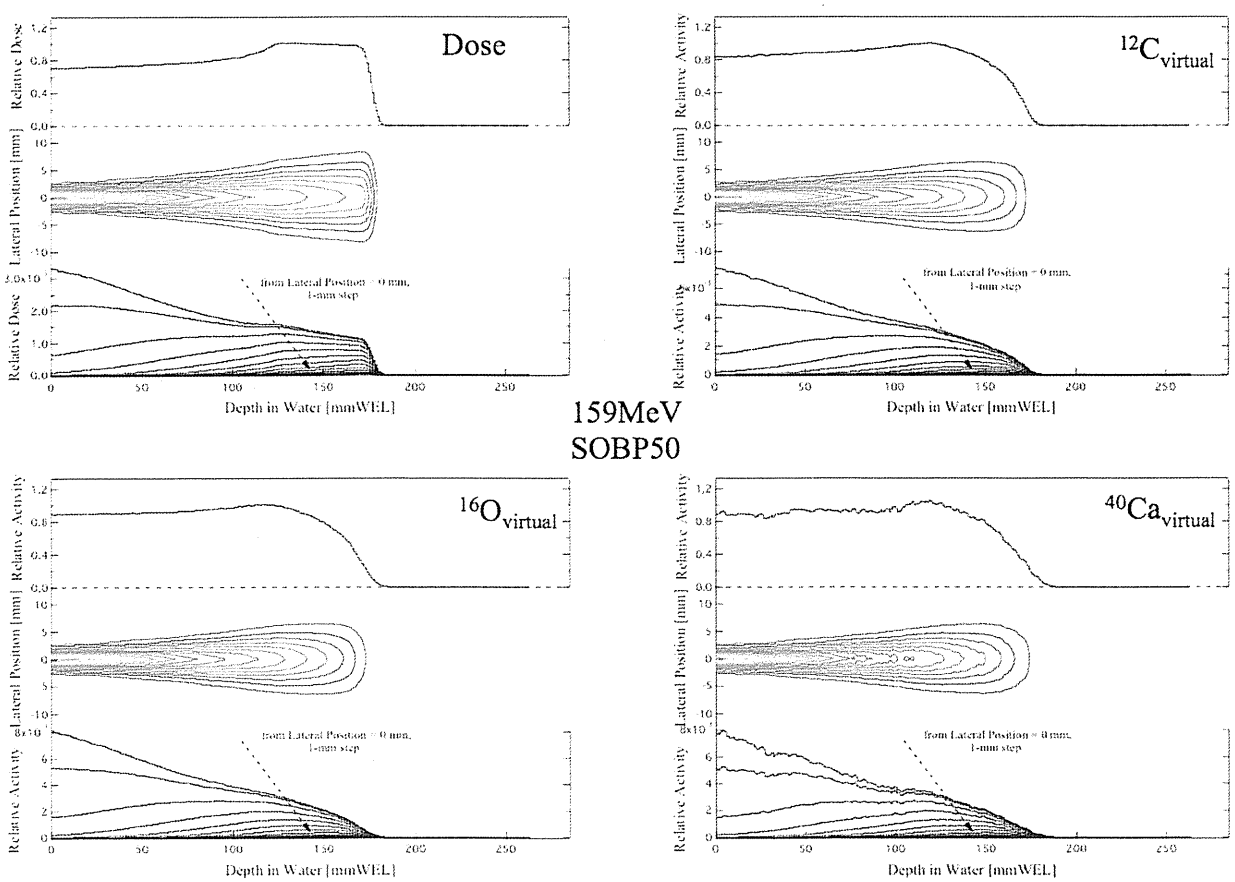

FIG. 6. The results of calculated dose and APB kernels of $^{12}C_{virtual}$, $^{16}O_{virtual}$, and $^{40}Ca_{virtual}$ with SOBP50-FD0-beam irradiation at 159 MeV. Each graph has three small graphs: (the upper) depth dose or activity distributions, (the middle) two-dimensional dose or APB kernels, and (the lower) depth dose or activity distributions toward the distance from the central proton beam axis.

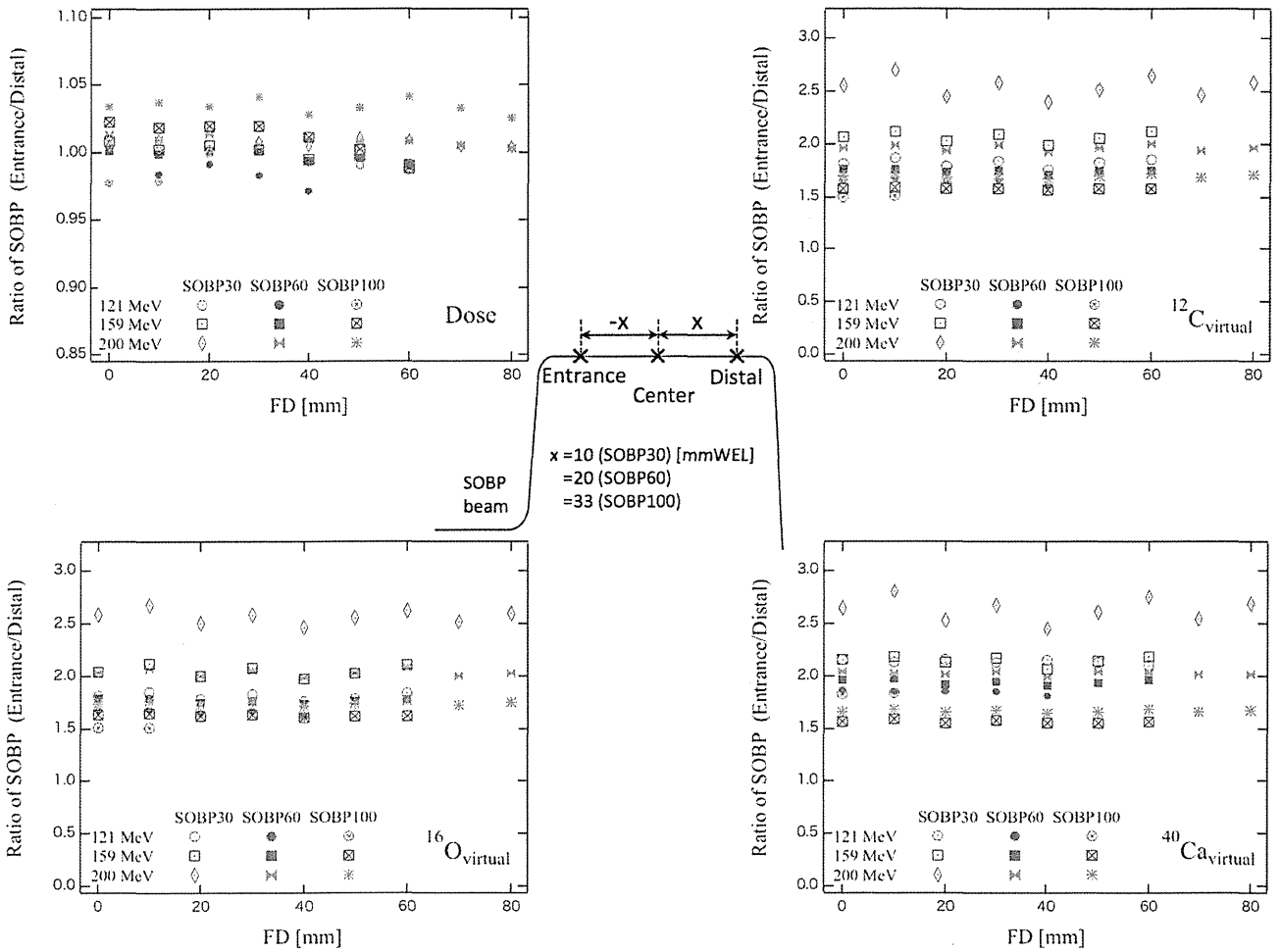

FIG. 7. Comparisons of dose distributions and SOBP_act of $^{12}C_{virtual}$, $^{16}O_{virtual}$, and $^{40}Ca_{virtual}$ in slopes of SOBP at three energies. An entrance was defined as the nearest point to an incident beam and a distal as the furthest point. The ratio of relative value (activity or dose) at the entrance to that at the distal was plotted with a parameter of FD thickness.

TABLE I. The degree of changes in SOBP's shape of SOBP_act toward that of dose distributions.

	R[a](activity distribution of virtual nucleus)/R[a](dose distribution)					
	SOBP30		SOBP60		SOBP100	
121 MeV	FD = 0	FD = 60	FD = 0	FD = 40	FD = 0	FD = 10
R($^{12}C_{virtual}$)/R(Dose)	1.8	1.9	1.7	1.7	1.5	1.5
R($^{16}O_{virtual}$)/R(Dose)	1.8	1.9	1.7	1.7	1.5	1.5
R($^{40}Ca_{virtual}$)/R(Dose)	2.1	2.1	1.9	1.9	1.9	1.9
159 MeV	FD = 0	FD = 60	FD = 0	FD = 60	FD = 0	FD = 60
R($^{12}C_{virtual}$)/R(Dose)	2.0	2.1	1.8	1.8	1.5	1.6
R($^{16}O_{virtual}$)/R(Dose)	2.0	2.1	1.8	1.8	1.6	1.6
R($^{40}Ca_{virtual}$)/R(Dose)	2.1	2.2	1.9	2.0	1.5	1.6
200 MeV	FD = 0	FD = 80	FD = 0	FD = 80	FD = 0	FD = 80
R($^{12}C_{virtual}$)/R(Dose)	2.5	2.6	1.9	1.9	1.6	1.7
R($^{16}O_{virtual}$)/R(Dose)	2.6	2.6	2.0	2.0	1.7	1.7
R($^{40}Ca_{virtual}$)/R(Dose)	2.6	2.7	2.0	2.0	1.6	1.6

[a]R: ratio of SOBP (entrance/distal).

beam through FD increases in the proton dose distribution. The change of slope of SOBP was verified every FD thickness in SOBP_act.

Values of relative activity or dose at verification points were analyzed in the dose distributions or calculated SOBP_act to verify changing slopes of SOBP. The verification points (entrance and distal) were set as ±10 mm WEL (SOBP30), ±20 mm WEL (SOBP60), and ±33 mm WEL (SOBP100) from a SOBP center point in a dose distribution under irradiation conditions of a certain energy, FD thickness, and SOBP width. Ratio between values at entrance and distal was calculated and Figure 7 shows the results of dose distributions and SOBP_act of three virtual nuclei at three energies. From this analysis, the lower the energy and the wider the SOBP width, the larger the degree of decline around beam entrance in SOBP became toward increasing of the FD thickness in dose distributions. In activity distributions, it was shown that the degree of each SOBP's slope was steeper than that in dose distributions.

The value was calculated from dividing the ratio of SOBP_act by that of dose distribution at each energy and SOBP width in order to clarify the change in SOBP's shape of SOBP_act toward that of the dose distribution. Table I shows these results of minimum and maximum FD thickness. The value of the ratio was about 2 to 3. In Table I, there were few changes of values with FD thickness increasing at one SOBP width and energy in every virtual nucleus. On the other hand, it was shown that the value of the ratio increased with narrower SOBP width and larger energy. Therefore, the coverage of irradiated volume in the activity distribution will become lower than that in the dose distribution around distal edge of SOBP. This tendency is more noticeable in narrower SOBP width and larger energy. And the predictive accuracy of the proton beam range in a patient will become low. It is very important for quality assurance of proton therapy to understand the differences between a dose distribution and an activity one.

4. CONCLUSIONS

A method to obtain SOBP_act using the measured MONO_act and material information of RF and the APB algorithm for SOBP beam irradiations were developed. It was proved that SOBP_act which is sorted in kind of nucleus, SOBP width, and thickness of FD could be reconstructed from measured MONO_act (with FD = 0) using the method within ±10% accuracy. Preparation of APB kernels of SOBP beams supports the use of a simulation system for imaging the clinical irradiated volume using the APB algorithm in clinical therapy with SOBP beams.

It was found that there were differences in the shapes of distributions in association with FD thickness and SOBP width between dose distributions and activity ones with SOBP beam irradiations. The possibility of estimating changes of ranges with FD thickness using a parameter of 50%-relative activity point (R_{act}) was suggested. The parameter (R_{act}) will be helpful to estimate the range of the beam in activity distributions resulting from a simulation using APB algorithm in the future.

Application of the simulation system to clinical proton therapy using SOBP beams is probably useful to provide treatments for patients with high accuracy. Comparison of the results of the measured data with those of the calculated data by the simulation system remains one of the important verifications to be carried out. The accuracy of calculation using the simulation system is under investigation. Our results in conjunction with *in vivo* dosimetry deserve further study.

ACKNOWLEDGMENTS

The authors would like to thank T. Okamoto of Hamamatsu Photonics K.K. for technical support. We also thank the staff members of the Proton Radiotherapy Department of the National Cancer Center, Kashiwa, for their help, and the members of SHI Accelerator Service Ltd. and Accelerator Engineering Inc. for the operation of the proton apparatus. This study was partially supported by grant-in-aid for Scientific Research (B) (23390308) and Health and Labor Sciences Research Grants (H22-Third Term Comprehensive Control Research for Cancer-025, H21-Clinical Research-006).

[a]Electronic mail: amiyatake@keenmp.co.jp

[1]T. Nishio, A. Miyatake, T. Ogino, K. Nakagawa, N. Saijo, and H. Esumi, "The development and clinical use of a beam ON-LINE PET system mounted on a rotating gantry port in proton therapy," Int. J. Radiat. Oncol., Biol., Phys. **76**, 277–286 (2010).

[2]T. Nishio, "Proton therapy facility at National Cancer Center, Kashiwa, Japan," J. At. Energy Soc. **41**, 1134–1138 (1999).

[3]T. Nishio, S. Kataoka, M. Tachibana, K. Matsumura, N. Uzawa, H. Saito, T. Sasano, M. Yamaguchi, and T. Ogino, "Development of a simple control system for uniform proton dose distribution in a dual-ring double scattering method," Phys. Med. Biol. **51**, 1249–1260 (2006).

[4]A. Miyatake, T. Nishio, T. Ogino, N. Saijo, H. Esumi, and M. Uesaka, "Measurement and verification of positron emitter nuclei generated at each treatment site by target nuclear fragment reactions in proton therapy," Med. Phys. **37**(8), 4445–4455 (2010).

[5]See http://www.nndc.bnl.gov/ for NNDC.

[6]ICRU, "Photon, electron, proton and neutron interaction date for body tissues," ICRU Report No. 46 (ICRU Publications, Washington, DC, 1992), pp. 11–13.

[7]A. Miyatake, T. Nishio, and T. Ogino, "Development of activity pencil beam algorithm using measured distribution data of positron emitter nuclei generated by proton irradiation of targets containing ^{12}C, ^{16}O, and ^{40}Ca nuclei in preparation of clinical application," Med. Phys. **38**(10), 5818–5829 (2011).

[8]G. W. Bennett, A. C. Goldberg, G. S. Levine, J. Guthy, and J. Balsamo, "Beam localization via 15O activation in proton-radiation therapy," Nucl. Instrum. Methods **125**, 333–338 (1975).

[9]U. Oelfke, G. Lam, and M. Atkins, "Proton dose monitoring with PET: Quantitative studies in Lucite," Phys. Med. Biol. **41**, 177–196 (1996).

[10]D. W. Litzenberg, D. A. Roberts, M. Y. Lee, K. Pham, A. M. Vander Molen, R. Ronningen, and F. D. Becchetti, "On-line monitoring of radiotherapy beams: Experimental results with proton beams," Med. Phys. **26**(6), 992–1006 (1999).

[11]K. Parodi, and W. Enghardt, "Potential application of PET in quality assurance of proton therapy," Phys. Med. Biol. **45**, N151–N156 (2000).

[12]T. Nishio, T. Ogino, M. Shimbo, S. Katsuta, S. Kawasaki, T. Murakami, T. Sato, Y. Kojima, K. Murakami, and H. Ikeda, "Distributions of β^+ decayed nucleus produced from the target fragment reaction in $(CH_2)n$ and patient liver targets by using a proton beam for therapy," Abstracts of the XXXIV PTCOG Meeting, Boston, MA (2001), pp. 15–16.

[13]K. Parodi, W. Enghardt, and T. Haberer, "In-beam PET measurements of β^+ radioactivity induced by proton beams," Phys. Med. Biol. **47**, 21–36 (2002).
[14]Y. Hishikawa, K. Kagawa, M. Murakami, H. Sasaki, T. Akagi, and M. Abe, "Usefulness of positron-emission tomographic images after proton therapy," Int. J. Radiat. Oncol., Biol., Phys. **53**, 1388–1391 (2002).
[15]T. Nishio, T. Sato, H. Kitamura, K. Murakami, and T. Ogino, "Distributions of β^+ decayed nuclei generated in the CH_2 and H_2O targets by the target nuclear fragment reaction using therapeutic MONO and SOBP proton beam," Med. Phys. **32**(4), 1070–1082 (2005).
[16]K. Parodi, F. Ponisch, and W. Enghardt, "Experimental study on the feasibility of in-beam PET for accurate monitoring of proton therapy," IEEE Trans. Nucl. Sci. **52**, 778–786 (2005).
[17]T. Nishio, T. Ogino, K. Nomura, and H. Uchida, "Dose-volume delivery guided proton therapy using beam ON-LINE PET system," Med. Phys. **33**(11), 4190–4197 (2006).
[18]K. Parodi, H. Paganetti, E. Cascio, J. B. Flanz, A. A. Bonab, N. M. Alpert, K. Lohmann, and T. Bortfeld, "PET/CT imaging for treatment verification after proton therapy: A study with plastic phantoms and metallic implants," Med. Phys. **34**(2), 419–435 (2007).
[19]K. Parodi, A. Ferrari, F. Sommerer, and H. Paganetti, "Clinical CT-based calculations of dose and positron emitter distributions in proton therapy using the FLUKA Monte Carlo code," Phys. Med. Biol. **52**, 3369–3387 (2007).
[20]K. Parodi, H. Paganetti, H. A. Shih, S. Michaud, J. S. Loeffler, T. F. Delaney, N. J. Liebsch, J. E. Munzenrider, A. J. Fischman, A. Knopf, and T. Bortfeld, "Patient study of in vivo verification of beam delivery and range, using positron emission tomography and computed tomography imaging after proton therapy," Int. J. Radiat. Oncol., Biol., Phys. **68**(3), 920–934 (2007).
[21]T. Nishio, A. Miyatake, K. Inoue, S. Katsuta, T. Gomi-Miyagishi, R. Kohno, S. Kameoka, K. Nakagawa, and T. Ogino, "Experimental verification of proton beam monitoring in a human body by use of activity image of positron-emitting nuclei generated by nuclear fragmentation reaction," Radiol. Phys. Technol. **1**(1), 44–54 (2008).
[22]T. Akagi, A. Higashi, H. Tsugami, H. Sakamoto, Y. Masuda, and Y. Hishikawa, "Ridge filter design for proton therapy at Hyogo Ion Beam Medical Center," Phys. Med. Biol. **48**, N301–N312 (2003).
[23]R. G. Lynch, and I. O. Dahl, "Approximations to multiple Coulomb scattering," Nucl. Instrum. Methods Phys. Res. B **58**, 6–10 (1991).

IOP PUBLISHING PHYSICS IN MEDICINE AND BIOLOGY

Phys. Med. Biol. **58** (2013) 1169–1184 doi:10.1088/0031-9155/58/4/1169

Application of the pencil-beam redefinition algorithm in heterogeneous media for proton beam therapy

Y Egashira[1], T Nishio[2], K Hotta[2], R Kohno[2] and M Uesaka[1]

[1] Department of Bioengineering, Graduate School of Engineering, University of Tokyo, 2-11-16, Yayoi, Bunkyo-ku, Tokyo 113-8656, Japan
[2] Particle Therapy Division, Research Centre for Innovative Oncology, National Cancer Centre, Kashiwa, 6-5-1 Kashiwanoha, Kashiwa-shi, Chiba 277-8577, Japan

E-mail: y.egashir@gmail.com

Received 10 October 2012, in final form 6 December 2012
Published 31 January 2013
Online at stacks.iop.org/PMB/58/1169

Abstract

In proton beam therapy, changes in the proton range due to lateral heterogeneity may cause serious errors in the dose distribution. In the present study, the pencil-beam redefinition algorithm (PBRA) was applied to proton beam therapy to address the problem of lateral density heterogeneity. In the calculation, the phase-space parameters were characterized for multiple range (i.e. proton energy) bins for given pencil beams. The particles that were included in each pencil beam were transported and redefined periodically until they had stopped. The redefined beams formed a detouring path that was different from that of the non-redefined pencil beams, and the path of each redefined beam was straight. The results calculated by the PBRA were compared with measured proton dose distributions in a heterogeneous slab phantom and an anthropomorphic phantom. Through the beam redefinition process, the PBRA was able to predict the measured proton-detouring effects. Therefore, the PBRA may allow improved calculation accuracy when dealing with lateral heterogeneities in proton therapy applications.

(Some figures may appear in colour only in the online journal)

1. Introduction

Pencil-beam (PB) algorithms (PBAs) (Hogstrom *et al* 1981, Petti 1992, Russell *et al* 1995, Hong *et al* 1996, Schaffner *et al* 1999, Russell *et al* 2000, Szymanowski *et al* 2001, Szymanoqski and Oelfke 2002) are among the most widely used models in the treatment planning of radiation therapy using charged particles (i.e. electron, proton, carbon ion, etc). In a homogeneous material, the accuracy of the PBA is satisfactory within a reasonable computing time. In a heterogeneous media, however, PBA calculations extremely limit its accuracy because of the central-axis approximation. Some particles included in such PBs may

0031-9155/13/041169+16$33.00 © 2013 Institute of Physics and Engineering in Medicine Printed in the UK & the USA

extend beyond the interface of the density heterogeneity. Several techniques for addressing the problem of lateral density heterogeneities have been introduced into the PBAs. Schaffner *et al* (1999) reduced the overreaching of protons by splitting each scanning beam into small virtual pencil beams for dose calculation on the patient surface. The central-axis semiinfinite slab approximation proposed by Szymanoqski and Oelfke (2002) introduced a supplementary scaling acting on the PB off-axis distribution. This two-dimensional density scaling of the PB calculation has also improved the calculation accuracy around lateral density heterogeneities.

For electron therapy, Shiu and Hogstrom (1991) proposed the PB redefinition algorithm (PBRA) to overcome the limitations of the semifinite slab approximation inherent in conventional PBA calculations. Boyd *et al* (2001) reported that the PBRA improved the electron dose calculation for heterogeneities in cases of simple phantom geometries. For beam transportation in the Fermi–Eyges theory (Eyges 1948), three physical quantities of the particles are used: the spatial variance $\overline{t^2}$, angular variance $\overline{\theta^2}$, and angular-spatial covariance $\overline{\theta t}$ (Hollmark *et al* 2004, Kanematsu *et al* 2008). The PBRA handles the particle flow and energy at each redefinition plane. The physical quantities are characterized for multiple energy bins for a given PB. A concept similar to the PBRA was applied to heavy particles for computational modelling of beam-customization devices such as collimators and a range compensator, in which particle flow in the transverse plane was considered in the absence of heterogeneity (Kanematsu *et al* 2008). Without residual range variation, in such geometry, the particles could not be distinguished from the PBs in terms of statistical parameters such as phase space parameters and number of particles. Modulated range loss and scattering effects from the range and human body prevented the application of the redefinition technique, due to the range variation of the PBs. Therefore, to improve the calculation accuracy of the redefinition technique, the particle flow in energy space should be considered.

We previously proposed the spatial resampling technique (SRPBA), which was a special case of the PBRA with one-dimensional (1D) density scaling and a limited number of redefinition planes (up to two) (Egashira *et al* 2012). This method improved the calculation accuracy of the proton dose distribution in simple geometries. However, proton energy degrades and scatters further out after beam redefinition, and such broadened PBs may overreach lateral borders of heterogeneities. Therefore, the depth of the second redefinition plane strongly affected its accuracy and performance. Moreover, some correlation factors were required to calculate the angular distribution of the particles included in the redefined PB, due to the use of 1D density scaling.

Protons, like electrons, gradually lose energy in a material because of their Coulomb collisions with atoms. Their rate of energy loss increases as their energy decreases. Protons have a Bragg peak in the human body, in which their scattering angle is smaller than that of electrons. In particular, in a passive scattering method, a patient-specific range compensator should be attached at the nozzle exit to achieve conformity of the proton dose. Protons drift between the range compensator and patient body, forming a complicated energy spectrum at the patient surface. The resultant dose is severely affected by the particle path until the particles are stopped. In the PBRA, the PB parameters are characterized for proton energy (i.e. residual range) bins for the given PBs. Particles in each PB are transported and redefined periodically until all of the protons are stopped. Beam transport based on the Fermi–Eyges theory may allow the interval between the redefinition planes to be determined arbitrarily without any correlation factors. The PBRA effectively restricts the size of the PBs and considers the irregular paths of protons along the human body, thereby addressing the problem of lateral density heterogeneity.

In addition to the accuracy, the computational time of the treatment planning system is also an important factor. Intrinsically, the PBRA is computationally demanding because it utilizes

multiple energy bins for PB transport and dose deposition. Whereas the SRPBA regulates the number of redefinition planes for fast computation, the use of multiple energy bins of the PBs in the PBRA may improve the accuracy. For clinical use, the PBRA for proton beam therapy should be implemented within a reasonable computation time.

The purpose of this study was to evaluate the PBRA with respect to managing lateral density heterogeneity, by performing measurements in a heterogeneous slab phantom and an anthropomorphic phantom for proton therapy. Additionally, a GPU-based calculation was applied to accelerate the performance of the PBRA for proton therapy.

2. Materials and methods

2.1. Proton PBRA

In this section, we briefly describe the PBRA that was originally proposed by Shiu and Hogstrom (1991). In the PBRA calculation for proton therapy, PBs are generated at the entrance to the range compensator. Subsequently, beam transport, beam redefinition, and dose deposition are periodically repeated until all of the particles that are included in the beam are stopped in the patient. In the calculations, the height of the isocentre is set to $z = 0$. Other coordinate systems are shown in figures 3 and 4.

2.1.1. Beam generation. Analogous to the PBA (Hong *et al* 1996, Szymanowski *et al* 2001), the effective source of the PBRA is approximated as a Gaussian, with a standard deviation of σ_{src} at a height $z = z_{\mathrm{src}}$. The mean direction of the protons for each PB, with slopes a_x and a_y, defines the fan lines from the effective source. Parameters that are related to the PB generation (Kanematsu *et al* 2008) are defined at the entrance to the range compensator at $z = z_c$, as follows:

$$x_{\mathrm{axis}\,ij} = x_j(z_c),\ y_{\mathrm{axis}\,ij} = y_i(z_c) \tag{1}$$

$$a_x(z_c)_{ij} = \frac{x_j(z_c)}{|z_c - z_{\mathrm{src}}|},\ a_y(z_c)_{ij} = \frac{y_i(z_c)}{|z_c - z_{\mathrm{src}}|} \tag{2}$$

$$\overline{\theta^2}_{ij}(z_c) = \frac{\sigma_{\mathrm{src}}^2}{(z_c - z_{\mathrm{src}})^2},\ \overline{\theta t}_{ij}(z_c) = \frac{\delta_{xy}^2}{12|z_c - z_{src}|},\ \overline{t^2}_{ij}(z_c) = \frac{\delta_{xy}^2}{12} \tag{3}$$

where $x_{\mathrm{axis}\,ij}$ and $y_{\mathrm{axis}\,ij}$ are the central axis positions of the PB_{ij} in x and y, respectively; and δ_{xy} is the calculation grid size. $R(z_c)$ is defined as the residual range at $z = z_c$. Inside the range compensator, the PBs are scattered from the effective scattering origin of the range compensator (Gottschalk *et al* 1993) and consecutively transported to the next plane.

2.1.2. Beam transport. During the transport of PBs in a material of interval Δz, parameter increments (Kanematsu 2009a) are calculated as follows:

$$\Delta x_{\mathrm{axis}\,ij} = a_{x\,ij}\Delta z,\ \Delta y_{\mathrm{axis}\,ij} = a_{y\,ij}\Delta z,\ \Delta s = \sqrt{a_{x\,ij}^2 + a_{y\,ij}^2 + 1}\cdot\Delta z \tag{4}$$

$$\Delta R = -WEL(\Delta s) \tag{5}$$

$$\Delta\overline{\theta^2} = 0.001\cdot\ln\frac{R}{R+\Delta R},\ \Delta\overline{\theta t} = \left(\overline{\theta^2} + \frac{1}{2}\Delta\overline{\theta^2}\right)\cdot\Delta s,$$
$$\Delta\overline{t^2} = \left[2\overline{\theta t} + \left(\overline{\theta^2} + \frac{1}{3}\Delta\overline{\theta^2}\right)\Delta s\right]\Delta s \tag{6}$$

where the water equivalent length of Δs ($WEL(\Delta s)$) corresponds to the range loss in the beam path Δs.

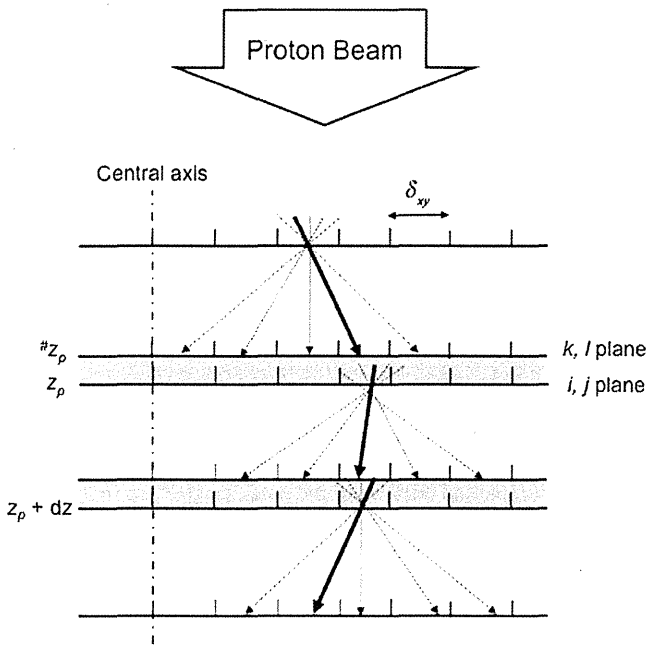

Figure 1. Illustration of the redefinition procedure: pencil beams are redefined at each depth, where the phase-space parameters should be recalculated.

2.1.3. Beam redefinition. The PB parameters need to be characterized for multiple energy (i.e. residual range) bins in a material. Figure 1 illustrate the beam redefinition in the patient plane $z = z_p$.

The plane $z = {}^{\#}z_p$ (i.e. k, l plane) is defined immediately upstream of the plane $z = z_p$ (i.e. i, j plane), where the PBs have not been redefined. In the PBRA calculation at $z = z_p$, the increment of the particles included in pixel (i, j, z_p) for the mth range (i.e. energy) bin $\left(\Delta N^{\#}_{k,l}\right)_m$ is defined as the contribution of particle numbers in pixel (i, j, z_p) from the pixel (k, l, $^{\#}z_p$) and is described as follows:

$$(\Delta N^{\#}_{k,l})_m = \sum_{\substack{n=1 \\ \in R_m \leqslant (\overline{R}^{\#}_{kl})_n < R_{m+1}}}^{R_b} (N^{\#}_{kl})_n \cdot \frac{1}{2}\left[\operatorname{erf}\left(\frac{(\Delta x^{\#})_n + \frac{\delta_{xy}}{2}}{\sqrt{2\left(\overline{t^2}^{\#}_{kl}\right)_n}}\right) - \operatorname{erf}\left(\frac{(\Delta x^{\#})_n - \frac{\delta_{xy}}{2}}{\sqrt{2\left(\overline{t^2}^{\#}_{kl}\right)_n}}\right)\right] \times \frac{1}{2}\left[\operatorname{erf}\left(\frac{(\Delta y^{\#})_n + \frac{\delta_{xy}}{2}}{\sqrt{2\left(\overline{t^2}^{\#}_{kl}\right)_n}}\right) - \operatorname{erf}\left(\frac{(\Delta y^{\#})_n - \frac{\delta_{xy}}{2}}{\sqrt{2\left(\overline{t^2}^{\#}_{kl}\right)_n}}\right)\right] \tag{7}$$

where $(N^{\#}_{kl})_n$ is the number of particles included in pixel (k, l, $^{\#}z_p$) for the nth range bin; R_b is the number of range bins; and$(\overline{R}^{\#}_{kl})_n$ is the residual range of protons falling in the mth range bin, which satisfies $R_m \leqslant (\overline{R}^{\#}_{kl})_n < R_{m+1}$. $(\Delta x^{\#})_n$ and $(\Delta y^{\#})_n$ are the distance between the central axis position of the PB and the calculation grid.